Optical Engineering

SPIEDigitalLibrary.org/oe

Data consistency condition–based beam-hardening correction

Shaojie Tang
Xuanqin Mou
Qiong Xu
Yanbo Zhang
James Bennett
Hengyong Yu

SPIE

Data consistency condition–based beam-hardening correction

Shaojie Tang
Xi'an University of Posts and Telecommunications
School of Automation
Xi'an, Shaanxi, 710121, China
and
Xi'an Jiaotong University
Institute of Image Processing and Pattern Recognition
Xi'an, Shaanxi, 710049, China

Xuanqin Mou
Qiong Xu
Yanbo Zhang
Xi'an Jiaotong University
Institute of Image Processing & Pattern Recognition
Xi'an, Shaanxi, 710049, China
E-mail: xqmou@mail.xjtu.edu.cn

James Bennett
Virginia Tech
VT-WFU School of Biomedical Engineering and Sciences
Biomedical Imaging Division
Blacksburg, Virginia 24061

Hengyong Yu
Wake Forest University Health Sciences
Department of Radiology
Division of Radiologic Sciences
Winston-Salem, North Carolina 27157
and
VT-WFU School of Biomedical Engineering and Sciences
Biomedical Imaging Division
Winston-Salem, North Carolina 27157

Abstract. In medical x ray computed tomography (CT) imaging devices, the x ray tube usually emits a polychromatic spectrum of photons resulting in beam-hardening artifacts in the reconstructed images. The bone-correction method has been widely adopted to compensate for beam-hardening artifacts. However, its correction performance is highly dependent on the empirical determination of a scaling factor, which is used to adjust the ratio of the reconstructed value in the bone region to the actual mass density of bone-tissue. A significant problem with bone-correction is that a large number of physical experiments are routinely required to accurately calibrate the scaling factor. In this article, an improved bone-correction method is proposed, based on the projection data consistency condition, to automatically determine the scaling factor. Extensive numerical simulations have verified the existence of an optimal scaling factor, the sensitivity of bone-correction to the scaling factor, and the efficiency of the proposed method for the beam-hardening correction. [DOI: 10.1117/1.3599869]

Subject terms: x ray computed tomography; polychromatic spectrum; beam-hardening; consistency condition.

Paper 100842RR received Oct. 14, 2010; revised manuscript received May 7, 2011; accepted for publication May 20, 2011; published online Jul. 25, 2011.

1 Introduction

Currently, computed tomography (CT) reconstruction is an important topic in medical imaging research. After several decades of effort, a large amount of reconstruction algorithms have been developed for sophisticated x ray source trajectories; however, most of these algorithms were constructed based on the assumption of an ideal monochromatic projection.[1–4] Yet, most medical x ray CT (XCT) devices emit a polychromatic spectrum of photons from their x ray sources, which result in a beam-hardening effect[5–11] and subsequent beam-hardening artifacts (e.g., cupping, streak, spillover, and pseudo cortex) in the reconstructed images.[5–8] It is well known that the beam-hardening effect is a dominant error source in medical XCT imaging and difficult to completely eliminate in practical applications. Clinical researchers have revealed that beam-hardening effect remains a critical degradation factor in current medical XCT imaging.[12,13]

Studies on beam-hardening correction have been launched since the invention of the medical XCT system by Hounsfield in the 1970's. Existing correction methods can be broadly categorized into three classes. At first, there is the so-called physical method class, which includes: water bag correction,[14] x ray source filter,[5,15] etc. The major characteristic of this class is that extra physical components are always required in the XCT systems. Second, there is the so-called pre-processing method class, which includes: water-correction,[5,6] sole-polynomial linearization,[6] bi-modals linearization for the special assembly of x ray source and detector,[16] empirical cupping correction (ECC),[17] etc. Most of the correction methods in this class are performed before the final CT image is reconstructed. Third, there is the so-called post-processing method class, which includes: bone-correction for the imaged objects of

0091-3286/2011/$25.00 © 2011 SPIE

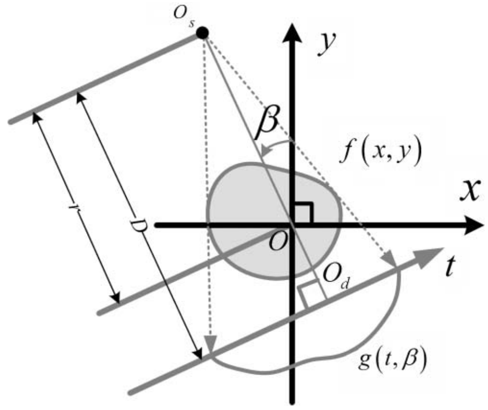

Fig. 1 Schematic of equispatial fan-beam geometry in CT imaging.

two-material components[7,8] or multimaterial components,[18] iteration between the projection space and the image space with a prior knowledge of polychromatic x ray spectrum,[19–21] bi-polynomial linearization,[22] Helgasson-Ludwig (H-L) consistency condition based corrections,[23–25] empirical beam-hardening correction (EBHC),[26] etc. The major characteristic of this class is that they are performed based on an initial reconstruction or image segmentation. Here, dual-energy XCT imaging is considered as a special case of the beam-hardening correction method.[27–29]

Among all the aforementioned correction methods, both the water-[5,6] and bone-correction[7,8] are the most classical techniques, and have been widely adopted in medical XCT systems. While it is convenient to implement these techniques, several drawbacks still remain. Water-correction can only correct for the imaged objects of a single-material component. Although bone-correction is useful for the imaged objects of two-material components, it cannot efficiently adapt to the different imaging conditions. The underlying reason for this complication is that the scaling factor, which is used to adjust the ratio of the reconstructed value in the bone region to the actual mass density of bone-tissue, routinely requires calibration.[7,8]

Meanwhile, the projection data consistency conditions have been utilized to solve several XCT problems.[30–39] Particularly, it was demonstrated that the beam-hardening correction based on the physical model of x ray imaging, and the H-L consistency condition, is feasible.[25] Inspired by previous investigations, in this article we will construct an objective function by combining the bone-correction formula with the H-L consistency condition, and optimize the objective function to automatically and stably determine the scaling factor and corresponding coefficient vector for beam hardening correction in polychromatic XCT imaging.

2 Theory

Let $f(x, y) \in C^{\infty}$ be an object function with a finite support. Denote the projection of $f(x, y)$ as $g(t, \beta)$ in the equispatial fan-beam geometry as shown in Fig. 1. The definition domain of $g(t, \beta)$ is $\{(t, \beta) \mid t \in \mathbb{R}, \beta \in [0, 2\pi)\}$. The distances from the x ray source O_s to the rotational center O and to the detector center O_d are referred to as r and D, respectively.

Let $S(\varepsilon)$ and $Q(\varepsilon)$ be the emitting energy spectrum of x ray source and the absorption energy spectrum of energy-integrating type x ray detector, respectively; and $\varepsilon \in [\varepsilon_{\min}, \varepsilon_{\max}]$ is the photon energy. The imaging process of an ideal monochromatic x ray source with a specific photon energy $\varepsilon_{\text{mono}} \in [\varepsilon_{\min}, \varepsilon_{\max}]$ can be modeled as

$$g \triangleq \ln \frac{S(\varepsilon_{\text{mono}})\, Q(\varepsilon_{\text{mono}})}{S(\varepsilon_{\text{mono}})\, Q(\varepsilon_{\text{mono}}) \exp[-\int_L \mu(l, \varepsilon_{\text{mono}})\, \rho(l)\, dl]}$$
$$= \int_L \mu(l, \varepsilon_{\text{mono}})\, \rho(l)\, dl, \tag{1}$$

where μ and ρ represent the mass attenuation coefficient and mass density of imaged object, respectively, and L denotes the integral line segment corresponding to an x ray path. Obviously, the H-L consistency condition in the appendix is satisfied by the object function $f(x, y) \triangleq \mu(x, y, \varepsilon_{\text{mono}})\, \rho(x, y)$ and its monochromatic projection g. Therefore, a general CT reconstruction algorithm, such as filtered back-projection (FBP),[40,41] applies to the monochromatic projection g.

In diagnostic XCT systems, the x ray source typically emits a polychromatic spectrum of photons. The imaging process of a polychromatic x ray source can be modeled as

$$\hat{g} \triangleq \ln \left\{ \int_{\varepsilon_{\min}}^{\varepsilon_{\max}} S(\varepsilon)\, Q(\varepsilon)\, d\varepsilon \Big/ \int_{\varepsilon_{\min}}^{\varepsilon_{\max}} S(\varepsilon)\, Q(\varepsilon) \right.$$
$$\left. \times \exp\left[-\int_L \mu(l, \varepsilon)\, \rho(l)\, dl \right] d\varepsilon \right\}. \tag{2}$$

In contrast to the monochromatic case, the H-L consistency condition is not satisfied by the object function $f(x, y) \triangleq \mu(x, y, \varepsilon_{\text{mono}})\, \rho(x, y)$ and its polychromatic projection $\hat{g}$. Therefore, beam-hardening artifacts[5–13] will appear in the images reconstructed by the FBP algorithm from the polychromatic projection $\hat{g}$.

Cupping artifacts will appear in the reconstructed images if the imaged object is "water-like" in its x ray attenuation characteristics. Water-correction with a specific correction polynomial can be used to compensate for the cupping artifacts[5,6] in two separate phases.[5,6] In the first phase, the water-equivalent material slabs, with diverse thicknesses, are used as the imaged objects to acquire the polychromatic projection $\hat{g}$. Meanwhile, the monochromatic projection g is calculated by using the model expressed in Eq. (1). Then, the correction polynomial is inversely solved to fit the polychromatic projection $\hat{g}$. The correction polynomial is used in the following form:

$$g \approx P_w(\hat{g}) \triangleq \sum_{n=0}^{N} a_n (\hat{g})^n. \tag{3}$$

In the second phase, the polychromatic projection $\hat{g}$ acquired in the imaging site is converted as $P_w(\hat{g})$ to approximate a monochromatic projection g, based on $\{a_n\}$ determined in the first phase. After water-correction, the FBP algorithm is used to process $P_w(\hat{g})$. It should be noted that the performance of water-correction typically correlates with the extent to which the imaged object is water-like.

When the bone- and soft-tissues simultaneously emerge in the field of view, streak and cupping artifacts will appear in the reconstructed images due to the significant difference in the x ray attenuation characteristics of bone- and soft-tissues. In this situation, bone-correction can be adopted to compensate for the cupping and streak artifacts.[7,8] At first, the polychromatic projection $\hat{g}$ is pre-processed by water-correction. Second, an image f_w is reconstructed from the water-corrected projection $P_w(\hat{g})$. Third, the image f_w is segmented into a soft-tissue image

$$f_s(x, y) \triangleq \begin{cases} f_w(x, y), f_w(x, y) < T, \\ 0, f_w(x, y) \geq T, \end{cases} \tag{4}$$

and a bone-tissue image

$$f_b(x, y) \triangleq \begin{cases} 0, f_w(x, y) < T, \\ f_w(x, y), f_w(x, y) \geq T, \end{cases} \tag{5}$$

by using a simple threshold T. Fourth, by re-projecting the images f_s, f_b and f_w, we obtain

$$g_s \triangleq \int\int_{(x,y)\in L} f_s(x, y) dx dy, \tag{6}$$

$$g_b \triangleq \int\int_{(x,y)\in L} f_b(x, y) dx dy, \tag{7}$$

and

$$g_w \triangleq \int\int_{(x,y)\in L} f_w(x, y) dx dy, \tag{8}$$

Finally, the polychromatic projection $\hat{g}$ is processed according to the following bone-correction formula[7] to approximate the monochromatic projection g,

$$g \approx P_w(\hat{g}) + g_w - P_w \left\{ \ln \left[\int_{\varepsilon_{\min}}^{\varepsilon_{\max}} S(\varepsilon) Q(\varepsilon) d\varepsilon \Big/ \int_{\varepsilon_{\min}}^{\varepsilon_{\max}} S(\varepsilon) Q(\varepsilon) e^{-\mu_s(\varepsilon) g_s - \mu_b(\varepsilon) g_b / \lambda_0} d\varepsilon \right] \right\}, \tag{9}$$

where the parameter λ_0 represents the scaling factor used in bone-correction. μ_s and μ_b denote the mass attenuation coefficients of ideal soft- and bone-tissues, respectively.

3 Methods

In order to avoid a physical calibration, a strategy should be designed to automatically determine the scaling factor. Obviously, it is hard to achieve this goal by solely utilizing the bone-correction formula [Eq. (9)] because both g and λ_0 are unknown. In this article, we combine the H-L consistency condition and the bone-correction formula [Eq. (9)] into the following objective function:

$$\Xi_0(g, \lambda_0) \triangleq \sum_d w_d \sum_\beta \left[\int_{-\infty}^{+\infty} (g - g_w) \left(\frac{tD}{\sqrt{D^2 + t^2}} \right)^d \times \frac{D^3}{(D^2 + t^2)^{1.5}} dt - \psi_\beta^d(\lambda_0) \right]^2, \tag{10}$$

with

$$\psi_\beta^d(\lambda_0) \triangleq \int_{-\infty}^{+\infty} \left(P_w(\hat{g}) - P_w \left\{ \ln \left[\int_{\varepsilon_{\min}}^{\varepsilon_{\max}} S(\varepsilon) Q(\varepsilon) d\varepsilon \Big/ \int_{\varepsilon_{\min}}^{\varepsilon_{\max}} S(\varepsilon) Q(\varepsilon) e^{-\mu_s(\varepsilon) g_s - \mu_b(\varepsilon) g_b / \lambda_0} d\varepsilon \right) \right] \right\} \times \left(\frac{tD}{\sqrt{D^2 + t^2}} \right)^d \frac{D^3}{\left(D^2 + t^2\right)^{1.5}} dt, \tag{11}$$

where $w_d \geq 0, d \in \mathbb{N}$ is the weight coefficient of the d^{th} order residual error term, and D is the distance from the x ray source O_s to the detector center O_d. Note that for simplicity we have omitted the dependency of projection on the x ray path $[t, \beta - \tan^{-1}(t/D)]$, and have integrated the H-L consistency condition into Eq. (10).

3.1 *Objective Function* $\mathbf{\Phi}_0(\lambda_0)$

Although an infinite number of schemes are available for the choice of weight coefficient set $\{w_d \geq 0, d \in \mathbb{N}\}$, the 0^{th} order residual error term is the most essential for the minimization of object function Ξ_0. Therefore, we will only discuss the case of $w_d \neq 0$ iff $d = 0$. In this case, the objective function Ξ_0 in Eq. (10) can be simplified as

$$\Theta_0(g, \lambda_0) \triangleq \sum_\beta \left[\int_{-\infty}^{+\infty} (g - g_w) \frac{D^3}{(D^2 + t^2)^{1.5}} dt - \psi_\beta^0(\lambda_0) \right]^2. \tag{12}$$

Because the monochromatic projection g naturally satisfies the H-L consistency condition, we can define

$$n_{0,0} \triangleq \int_{-\infty}^{+\infty} g \frac{D^3}{(D^2 + t^2)^{1.5}} dt, \tag{13}$$

which is independent of the view-angle β, according to Eq. (A5) in the appendix. In this way, the unknown g is converted as $n_{0,0}$, and the number of unknowns is decreased dramatically. Meanwhile, the H-L consistency condition is also satisfied by g_w, which is the projection acquired by re-projecting the image f_w. So, we can define

$$n_{0,0}^w \triangleq \int_{-\infty}^{+\infty} g_w \frac{D^3}{(D^2 + t^2)^{1.5}} dt, \tag{14}$$

which is also independent of the view-angle β. Note that both g_w and $n_{0,0}^w$ are known, and the substitution in Eq. (14) is for the convenience of expression (see below). In this way, the objective function Θ_0 can be further simplified as

$$\mathbf{\Psi}_0(n_{0,0}, \lambda_0) \triangleq \sum_\beta \left(n_{0,0} - n_{0,0}^w - \psi_\beta^0(\lambda_0)\right)^2. \tag{15}$$

Unfortunately, if the imaged object is nearly rotationally symmetric around the rotational axis of the XCT system, the minimization of the objective function $\mathbf{\Psi}_0$ will be unstable. Therefore, the number of unknowns in the objective function

$\boldsymbol{\Psi}_0$ should be further reduced. To meet this goal, we designed a novel objective function

$$\boldsymbol{\Phi}_0(\lambda_0) \triangleq \sum_{\beta_1}\sum_{\beta_2}\left(\psi^0_{\beta_1}(\lambda_0) - \psi^0_{\beta_2}(\lambda_0)\right)^2, \beta_1, \beta_2 \in [0, 2\pi), \tag{16}$$

by mutually subtracting the residual terms of the different view-angle β in Eq. (15). In this article, $\boldsymbol{\Phi}_0(\lambda_0)$ is the final form of the objective function used to automatically determine the scaling factor λ_0.

3.2 *Objective Function* $\boldsymbol{\Phi}_1(\boldsymbol{c})$

If it is not easy to determine the spectrum data $S(\varepsilon)$ or $Q(\varepsilon)$, the term $\psi^d_\beta(\lambda_0)$ in the objective function $\boldsymbol{\Phi}_0$ can be approximated by an algebraic polynomial of g_s and g_b as follows,

$$\psi^d_\beta(\boldsymbol{c}) \triangleq \int_{-\infty}^{+\infty}\left\{P_w(\hat{g}) - \left[\, g_s\ g_b\ g_s^2\ g_b^2\ g_sg_b\ g_b^{0.5}\,\right]\cdot \boldsymbol{c}'\right\} \times \left(\frac{tD}{\sqrt{D^2+t^2}}\right)^d \frac{D^3}{(D^2+t^2)^{1.5}}dt, \tag{17}$$

where $c \triangleq [\, c_1\ c_2\ c_3\ c_4\ c_5\ c_6\,]$ is the coefficient vector corresponding to the scaling factor λ_0. The term $g_b^{0.5}$ is empirically added into the algebraic polynomial to increase the approximation accuracy. Note that the scaling factor λ_0 has been absorbed by the coefficient vector c, and $\psi^d_\beta(\lambda_0)$ is converted into $\psi^d_\beta(\boldsymbol{c})$. Therefore, Eq. (16) will be converted as

$$\boldsymbol{\Phi}_1(\boldsymbol{c}) \triangleq \sum_{\beta_1}\sum_{\beta_2}\left(\psi^0_{\beta_1}(\boldsymbol{c}) - \psi^0_{\beta_2}(\boldsymbol{c})\right)^2, \beta_1, \beta_2 \in [0, 2\pi). \tag{18}$$

In this article, $\boldsymbol{\Phi}_1(\boldsymbol{c})$ is the final form of the objective function used to automatically determine the coefficient vector c.

3.3 *Numerical Implementations*

To numerically implement the minimization of the aforementioned objective functions, we re-express the objective function $\boldsymbol{\Phi}_0(\lambda_0)$ as

$$\boldsymbol{\Phi}_0(\lambda_0) \triangleq \sum_{j=1}^{\max j}(\phi_j(\lambda_0))^2, \tag{19}$$

where $\phi_j(\lambda_0) \triangleq \psi^0_{\beta_1}(\lambda_0) - \psi^0_{\beta_2}(\lambda_0)$, the subscript j is the index of the combination of view angles β_1 and β_2, and $\max j$ can be determined by Eq. (16). Because $\phi_j(\lambda_0)$ is a nonlinear function of the variable λ_0, a nonlinear least-square method is required to minimize $\boldsymbol{\Phi}_0(\lambda_0)$ as follows:

$$\lambda_0^{k+1} \triangleq \lambda_0^k - (A_k'A_k)^{-1}A_k'\boldsymbol{\phi}^k, \tag{20}$$

where

$$A_k \triangleq \left[\,\nabla\phi_1\left(\lambda_0^k\right)\ \nabla\phi_2\left(\lambda_0^k\right)\ \cdots\ \nabla\phi_{\max j}\left(\lambda_0^k\right)\right]', \tag{21}$$

$$\boldsymbol{\phi}^k \triangleq \left[\,\phi_1\left(\lambda_0^k\right)\ \phi_2\left(\lambda_0^k\right)\ \cdots\ \phi_{\max j}\left(\lambda_0^k\right)\right]', \tag{22}$$

λ_0^k is the k^{th} step of approximation for the minimum value point of $\boldsymbol{\Phi}_0(\lambda_0)$. The iteration process will be terminated as soon as certain stopping criteria are satisfied. In this article, a maximal iteration number $\max k$ is used as the stopping criterion. Finally, the determined $\lambda_0^{\max k}$ is substituted into the following bone-correction formula for beam-hardening correction,

$$g \approx P_w(\hat{g}) + g_w - P_w\left\{\ln\left[\int_{\varepsilon_{\min}}^{\varepsilon_{\max}} S(\varepsilon)\,Q(\varepsilon)\,d\varepsilon \Big/ \int_{\varepsilon_{\min}}^{\varepsilon_{\max}} S(\varepsilon)\,Q(\varepsilon)\,e^{-\mu_s(\varepsilon)g_s-\mu_b(\varepsilon)g_b/\lambda_0^{\max k}}d\varepsilon\right]\right\}. \tag{23}$$

Similarly, the objective function $\boldsymbol{\Phi}_1(\boldsymbol{c})$ is re-expressed as

$$\boldsymbol{\Phi}_1(\boldsymbol{c}) \triangleq \sum_{j=1}^{\max j}(\phi_j(\boldsymbol{c}))^2. \tag{24}$$

where $\phi_j(\boldsymbol{c}) \triangleq \psi^0_{\beta_1}(\boldsymbol{c}) - \psi^0_{\beta_2}(\boldsymbol{c})$, and $\max j$ can be determined by Eq. (18). Because $\phi_j(\boldsymbol{c})$ is a linear function of the variable c, a linear least-square method can be adopted to minimize $\boldsymbol{\Phi}_1(\boldsymbol{c})$ as follows:

$$\boldsymbol{c}^1 \triangleq \boldsymbol{c}^0 - (A_0'A_0)^{-1}A_0'\boldsymbol{\phi}^0, \tag{25}$$

where

$$A_0 \triangleq [\,\nabla\phi_1(\boldsymbol{c}^0)\ \nabla\phi_2(\boldsymbol{c}^0)\ \cdots\ \nabla\phi_{\max j}(\boldsymbol{c}^0)\,]', \tag{26}$$

$$\boldsymbol{\phi}^0 \triangleq [\,\phi_1(\boldsymbol{c}^0)\ \phi_2(\boldsymbol{c}^0)\ \cdots\ \phi_{\max j}(\boldsymbol{c}^0)\,]', \tag{27}$$

$$\boldsymbol{c}^0 \triangleq 0. \tag{28}$$

Finally, the determined $\boldsymbol{c}^1$ is adopted for beam-hardening correction as follows:

$$g \approx P_w(\hat{g}) + g_w - \left[\, g_s\ g_b\ g_s^2\ g_b^2\ g_sg_b\ g_b^{0.5}\,\right]\cdot(\boldsymbol{c}^1)'. \tag{29}$$

4 Results

4.1 *Mechanical Parameters*

Previously, we have developed an in-house software to simulate the generation of projection data acquired in medical XCT systems.[11] In this article, the software is used to demonstrate the feasibility of our proposed method. We simulate an x ray circular scanning trajectory with a radius r of 50 cm, located in the $O-xy$ plane. A linear detector is positioned opposite to the x ray source O_s about the origin O, and the distance D from the x ray source to the detector center is 100 cm. The linear detector consists of 850×1 cells with an area of 1×1 mm^2 for each cell; 1080 projections are uniformly acquired for a full scan.

4.2 *X ray Spectrum*

To simulate the generation of projection data,[11] the emitting spectrum of the x ray source $S(\varepsilon)$ [see Fig. 2(a)][42] and the absorption spectrum of CsI x ray detector $Q(\varepsilon)$ (see Fig. 2(b))[43] are given. The spectra used for the projection simulation and beam-hardening correction are completely the same. In this article, we only assess the performance of beam-hardening correction itself. We also assume that no scattered photons reach the surface of the x ray detector, because the scattering component is negligible in the fan-beam

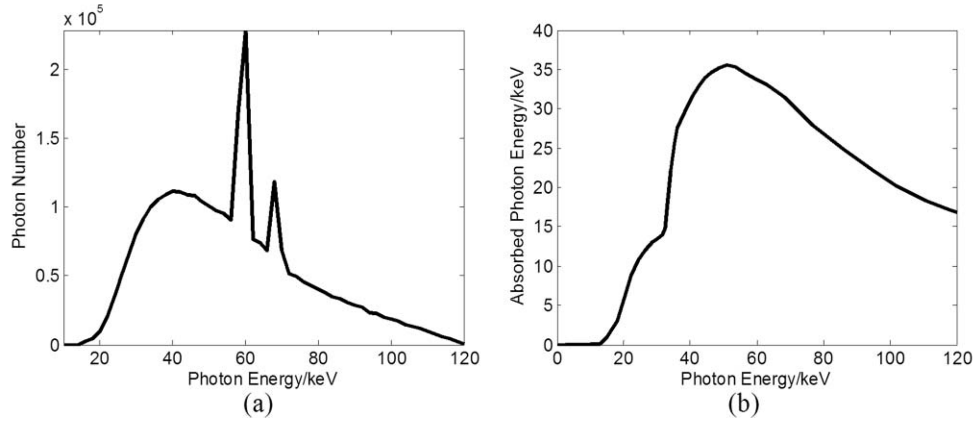

Fig. 2 (a) Emitting spectrum of x ray source and (b) absorption spectrum of CsI energy-integrating type x ray detector.

geometry. An energy sampling interval of 1 keV is used for the numerical computation of the polychromatic projection data. The tube potential is set as 120 kVp for the polychromatic case. Meanwhile, a monochromatic case of 66 keV is simulated to serve as a benchmark; the photon energy 66 keV is viewed as the effective energy of the polychromatic x ray source.

4.3 *Image Reconstruction*

In numerical simulation, the mathematical FORBILD head phantom[44] is adopted as an assumed imaged object, whose cross-section at $z = 0$ is shown in Fig. 3. The FBP algorithm is employed for the image reconstruction.[40,41] The reconstructed image is in a matrix of 512×512 pixels, with an area of 0.5×0.5 mm^2 for each pixel. To follow the convention in clinical XCT research, the reconstructed image is further converted as:

$$I(x, y) \triangleq \frac{f(x, y) - f_{\text{pw}}}{f_{\text{pw}}} \times 1000, \tag{30}$$

where $f(x, y)$ is the reconstructed image (i.e., the linear attenuation coefficient of imaged object) in 1/mm, f_{pw} is the average linear attenuation coefficient of pure water in 1/mm, and $I(x, y)$ is in Hounsfield units (HU).

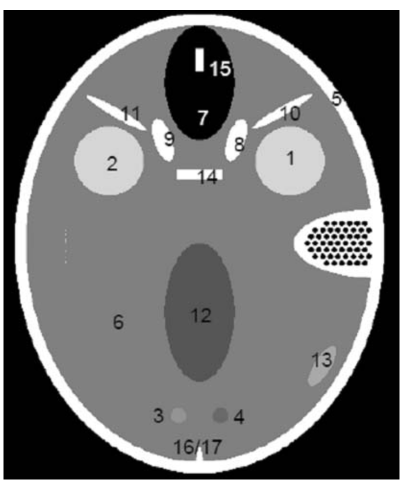

Fig. 3 Cross-section of the FORBILD head phantom at $z = 0$ and the labels of main sub-regions.

4.4 *Existence Validation of Optimal Scaling Factor*

To validate the existence of an optimal scaling factor, the effect of varying the scaling factor on the performance of bone-correction is quantitatively analyzed. For this purpose, an inconsistency error index is first defined as follows:

$$\gamma \triangleq \frac{\sum_{(x,y)\in R_N} |f(x, y) - m|}{N f_{\text{pw}}} \times 1000, \tag{31}$$

$$m \triangleq \sum_{(x,y)\in R_N} f(x, y)/N, \tag{32}$$

where γ is the inconsistency error in HU, and R_N represents a region of interest covering N pixels. The curves of the inconsistency error γ versus scaling factor λ_0 are plotted to demonstrate the existence of an optimal scaling factor for bone-correction. We select two regions, whose CT numbers are 800 and 50 HU in the original definition of the FORBILD head phantom, and name them as the bone- and soft-tissue regions, respectively. Various imaging conditions are simulated with two noise intensities (i.e., zero noise, and noise simulated with 3×10^6 photons per x ray path following a Poisson distribution) and four cross-sections (i.e., $z = 0$, $z = 5$ mm, $x = 0$, and $x = -67$ mm). These four cross-sections differ remarkably from each other as shown in Fig. 4.

In Figs. 5 and 6, the inconsistency error curves of the bone-corrected results are plotted with various imaging conditions. In Fig. 7, the objective function $\mathbf{\Phi}_0(\lambda_0)$ is also plotted with various imaging conditions. From these figures, it can be seen that an optimal scaling factor does exist, which shows a solid basis for the feasibility of our proposed method. Three optimal scaling factors were determined with various imaging conditions as listed in Table 1 and shown in Fig. 8. Therein, λ_b and λ_s denote the optimal scaling factors determined from Figs. 5 and 6 in the bone- and soft-tissue regions, respectively, while λ_0^{opt} denotes the optimal scaling factor determined from the objective function $\mathbf{\Phi}_0(\lambda_0)$ in Fig. 7. From Table 1 and Fig. 8, it can be noticed that λ_s is always larger than λ_b for the same imaging conditions, and the deviation of λ_s is larger than that of λ_b. In contrast to both λ_b and λ_s, the deviation of λ_0^{opt} is the lowest, and λ_b is very robust to noise effects. Here, it should be emphasized that these three optimal scaling factors λ_b, λ_s, and λ_0^{opt} are determined by exhaustively seeking with a finer interval. Therefore, the seeking scheme

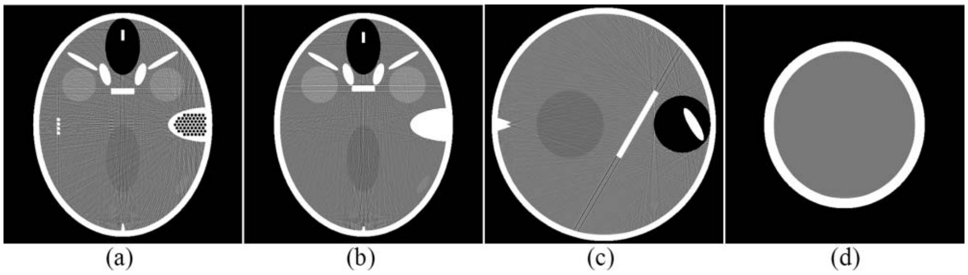

Fig. 4 Images reconstructed from the monochromatic projections of FORBILD head phantom at the positions of (a) $z = 0$, (b) $z = 5$ mm, (c) $x = 0$, and (d) $x =$ -67 mm.

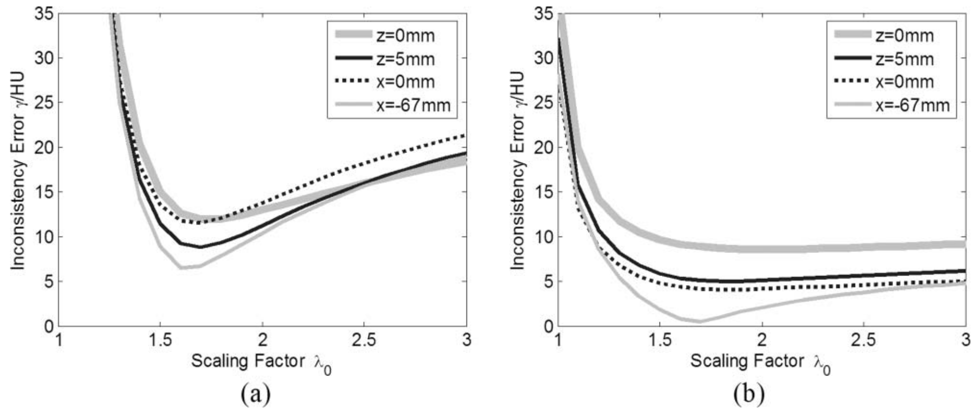

Fig. 5 Inconsistency error versus scaling factor λ_0 in the regions of (a) bone-tissue and (b) soft-tissue with noise-free polychromatic projection after bone-correction.

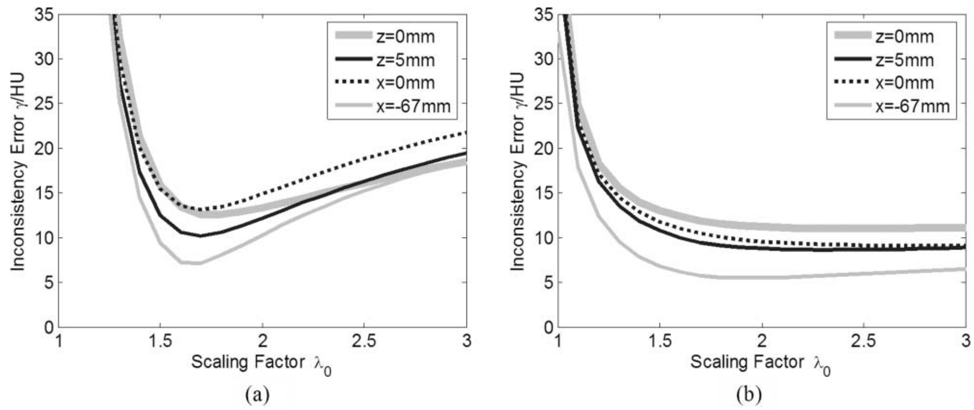

Fig. 6 Same as in Fig. 5 but with noisy polychromatic projection.

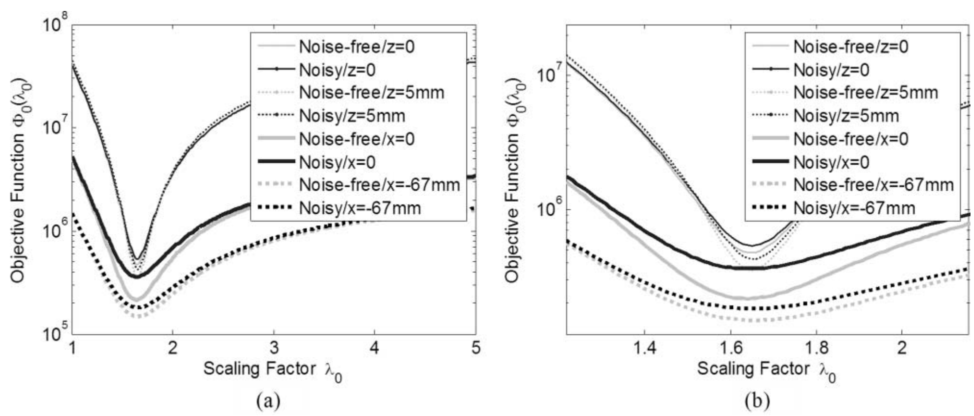

Fig. 7 Objective function $\Phi_0\,(\lambda_0)$ versus scaling factor λ_0. (b) is magnified from (a).

Table 1 Optimal scaling factors λ_b in the bone-tissue region and λ_s in the soft-tissue region determined from Figs. 5 and 6, and λ_0^{opt} determined from Fig. 7.

Position/mm		$z=0$	$z=5$	$x=0$	$x=-67$
λ_b	Noise-free	1.7006	1.6721	1.6428	1.6318
	Noisy	1.7572	1.6857	1.7002	1.6533
λ_s	Noise-free	1.9361	1.7705	1.7689	1.6697
	Noisy	2.4127	2.3064	2.7232	1.9236
λ_0^{opt}	Noise-free	1.6464	1.6506	1.6386	1.6571
	Noisy	1.6497	1.6531	1.6414	1.6514

could not be adopted in real-world applications, whereas our proposed method is more practicable as illustrated later.

4.5 *Performance Analysis of Correction Algorithms*

For convenience, hereafter we have fixed the cross-section at $z = 0$. The convergence speed and solution stability of our proposed method are studied with various noise intensities. In polychromatic XCT imaging, varying the number of photons substantially changes the signal to noise ratio in the reconstructed images and the dose delivered to the imaged object. For the minimization of objective function $\mathbf{\Phi}_0(\lambda_0)$, we set the max k as 9, and λ_0^0 (the initial value of scaling factor λ_0) as 1. The bone-corrections with $\lambda_0^{\max k}$ and $\boldsymbol{c}^1$ are compared to those with λ_b and λ_s.

From Fig. 9, it can be observed that the minimization process of the objective function $\mathbf{\Phi}_0(\lambda_0)$ converges faster for all imaging conditions. Noise effects have almost no influence on the convergence stability; especially, the $\lambda_0^{\max k}$ determined in Fig. 9(b) is almost the same as the λ_0^{opt} at cross-section $z = 0$ (see Fig. 8 and Table 1). Figure 10 shows the effect of varying the number of photons on the scaling factors and the objective functions. These results indicate that our proposed method is very robust to noise effects that is a crucial feature, given that noise effects always occur in real-world imaging conditions. From Fig. 10(a), we learn that λ_b approaches $\lambda_0^{\max k}$ and is also very robust to noise effects; however, λ_s is always much larger than λ_b and $\lambda_0^{\max k}$, and readily degraded by noise effects. From Fig. 10(b), we notice that $\mathbf{\Phi}_0(\lambda_0^{\max k})$ approaches $\mathbf{\Phi}_1(\boldsymbol{c}^1)$, while $\mathbf{\Phi}_0(\lambda_b)$ is near $\mathbf{\Phi}_0(\lambda_s)$. The results in Figs. 10(a) and 10(b) seem contradictory; however, it can be explained by the results in Figs. 5–8 and Table 1. That is, the objective function $\mathbf{\Phi}_0(\lambda_0)$ is much more sensitive to the scaling factor λ_0 than the inconsistency error index γ. At the same time, the minimum value point of the objective function $\mathbf{\Phi}_0(\lambda_0)$ is much more stable to the influences of both noise effects and cross-sectional position as compared to the inconsistency error index γ. Furthermore, it is impossible to exactly evaluate the optimal scaling factors, λ_b and λ_s, in real-world applications, as in Figs. 5 and 6 and Table 1. All these facts have demonstrated the superior characteristics of our proposed method.

As compared $\mathbf{\Phi}_1(\boldsymbol{c}^1)$ to $\mathbf{\Phi}_0(\lambda_0^{\max k})$ in Fig. 10(b), it seems to imply that the bone-correction with $\boldsymbol{c}^1$ is slightly superior to that with $\lambda_0^{\max k}$. This point will be further checked by evaluating the respective inconsistency errors γ in the Sec. 4.6.

4.6 *Performance Analysis of the Corrected Results*

In this subsection, the correction performance for the cupping and streak artifacts are studied with various noise intensities. The polychromatic images after various beam-hardening corrections are compared with the monochromatic image. Simultaneously, the influence of the scaling factor is illustrated by using the corrected images, and the visibility of subdural hematoma phenomenon is also discussed by using the profiles of the reconstructed images.

Figures 11 and 12 show the polychromatic images with various beam-hardening corrections, along with the difference images between these polychromatic images and the monochromatic image. These figures indicate that all correction methods are efficient for cupping artifacts. To evaluate the correction performance for streak artifacts, we focus on the region between the sub-region 14 and the right ear in the cross-section at $z = 0$ (as labeled in Fig. 3). In this region, the performance of water-correction is very limited, as illustrated by the severe dark streaks in the water-corrected images [Figs. 11(c) and 12(d)], and difference images [Figs. 11(d) and 12(d)]. The intensities of the dark streaks are almost the same as those in the uncorrected polychromatic images [Figs. 11(a) and 12(a)] and difference images [Figs. 11(b) and 12(b)]. The bone-correction with $\lambda_0 = 1.4$ gives an over-correction, which is illustrated by the bright streak artifacts in the images [Fig. 11(e) and 12(e)] and the difference images [Figs. 11(f) and 12(f)]. On the contrary, the 400 bone-correction with $\lambda_0 = 2.0$ offers an insufficient

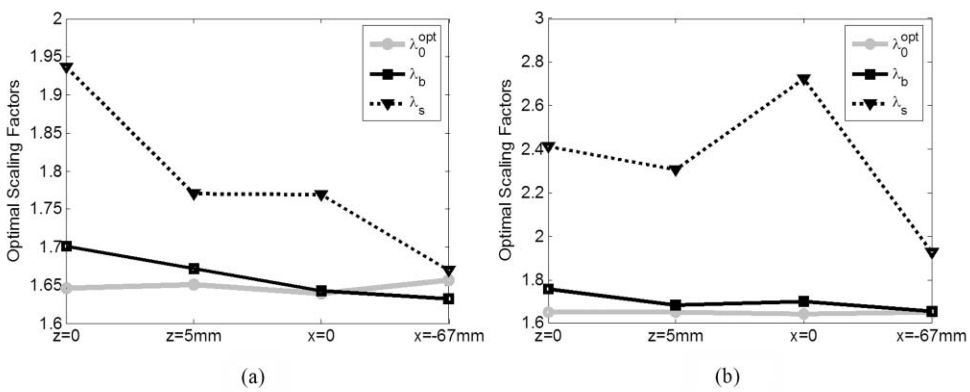

Fig. 8 Optimal scaling factors λ_0^{opt}, λ_b, and λ_s from (a) noise-free and (b) noisy projections.

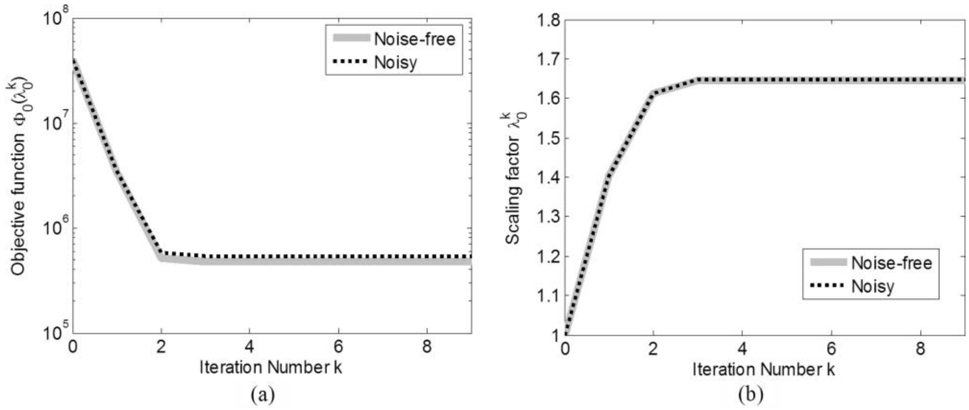

Fig. 9 Performance of objective function minimization. (a) Object function Φ_0 (λ_0^k) and (b) scaling factor λ_0^k versus iteration number *k*.

correction, which is shown by the slightly dark streak artifacts in the images [Figs. 11(g) and 12(g)] and difference images [Figs. 11(h) and 12(h)]. As shown in the images [Figs. 11(i)–11(l) and 12(i)-12(l)], our proposed method has a superior correction performance, and there are almost no residual cupping and streak artifacts remaining. Comparing the noise-free images in Fig. 11 and the noisy images in Fig. 12, it can be noticed that our proposed method is very robust to noise effects.

In Figs. 13 and 14 are the profiles of the monochromatic reconstruction, polychromatic reconstruction, water-corrected reconstruction, and various bone-corrected reconstructions (with $\lambda_0 = 1.4$, $\lambda_0 = 2.0$, $\lambda_0^{\max k}$, and $\boldsymbol{c}^1$). For simplicity, these reconstructions are denoted as Mono, Poly, Water, Bone:1.4, Bone:2.0, Bone:$\lambda_0^{\max k}$ and Bone:$\boldsymbol{c}^1$, respectively. As for the bone-corrections with λ_b and λ_s, we will denote them as Bone:λ_b and Bone: λ_s. In Figs. 13(a) and 14(a), the profiles are taken along the horizontal 215th line, which crosses the soft-tissue region between the sub-region 14 and the right ear. In Figs. 13(b) and 14(b), the profiles are taken along the horizontal 385th line to evaluate the visibility of the subdural hematoma in the sub-region 13. In Figs. 13(a) and 14(a), the performance of water-correction is very limited (profiles are very similar to those of uncorrected polychromatic reconstructions); the profile values of the bone-correction with $\lambda_0 = 1.4$ are slightly higher than the monochromatic reconstruction, and the profile values of the bone-correction with $\lambda_0 = 2.0$ are slightly lower than the monochromatic reconstruction. In Figs. 13(b) and 14(b), the performance of water-correction is still unsatisfactory; from the 395th to the 405th pixel, the profile values of the bone-correction with $\lambda_0 = 1.4$ are slightly lower than the monochromatic reconstruction, and the profile values of the bone-correction with $\lambda_0 = 2.0$ are significantly closer to the monochromatic reconstructions. On the contrary, the profile values of the bone-corrections with $\lambda_0^{\max k}$ and $\boldsymbol{c}^1$ are much closer to the monochromatic reconstruction.

From Figs. 13 and 14, it is observed that our proposed method is very robust to noise effects. In summary, the conclusions made from Figs. 13 and 14 are consistent with the analysis from Figs. 11 and 12. All the results show that the bone-correction method is sensitive to the choice of scaling factor, and the proposed method is feasible and can be used to automatically determine the scaling factor and corresponding coefficient vector.

In order to quantitatively analyze and compare the correction performance, we calculate the inconsistency errors in both the bone- and soft-tissue regions, for the reconstructed images in Figs. 11 and 12. The calculated inconsistency errors are listed in Table 2, from which we can see that the bone-correction with $\lambda_0^{\max k}$ can get a superior consistency in each region, while the bone-correction with $\boldsymbol{c}^1$ can also achieve an acceptable consistency, at least in the soft-tissue region (considering the lack of spectra data). Meanwhile, as we expect, the inconsistency error in the noise-free reconstruction is always lower than in the noisy one, while

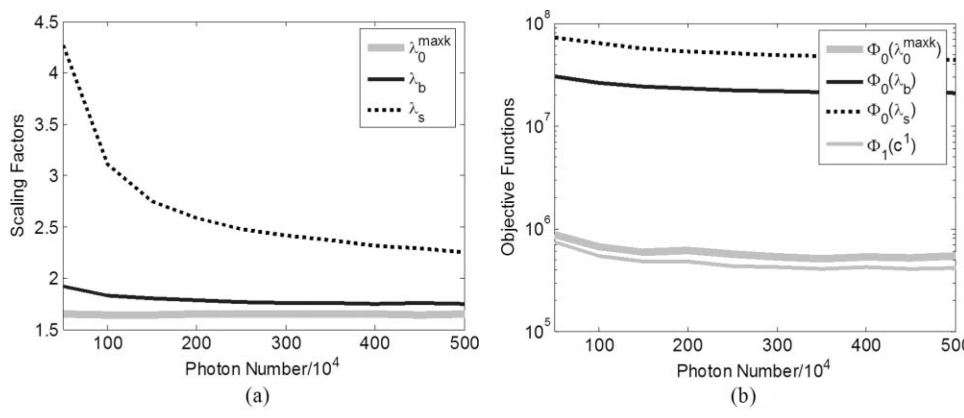

Fig. 10 Performance of objective function minimization. (a) Scaling factors and (b) objective functions versus the number of photons.

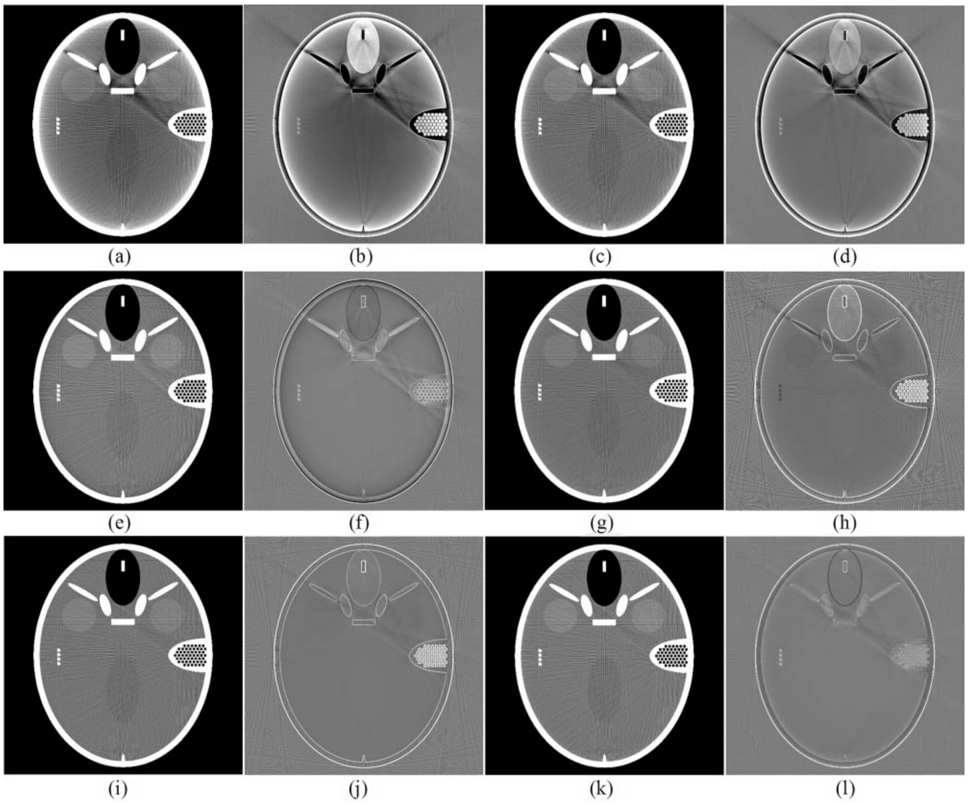

Fig. 11 Reconstructed images at $z = 0$ from noise-free polychromatic projection. (a) is the uncorrected polychromatic reconstruction, (c) is water-corrected reconstruction, (e) and (g) are the bone-corrected reconstructions with $\lambda_0 = 1.4$ and $\lambda_0 = 2.0$, and (i) and (k) are the bone-corrected reconstructions with $\lambda_0^{\max k}$ and $\boldsymbol{c}^1$. (b), (d), (f), (h), (j), (l) are the differences between (a), (c), (e), (g), (i), (k) and monochromatic reconstruction [Fig. 4(a)], respectively. While the reconstructed images are displayed within a window of [0 167] HU, the difference images [-34 34] HU.

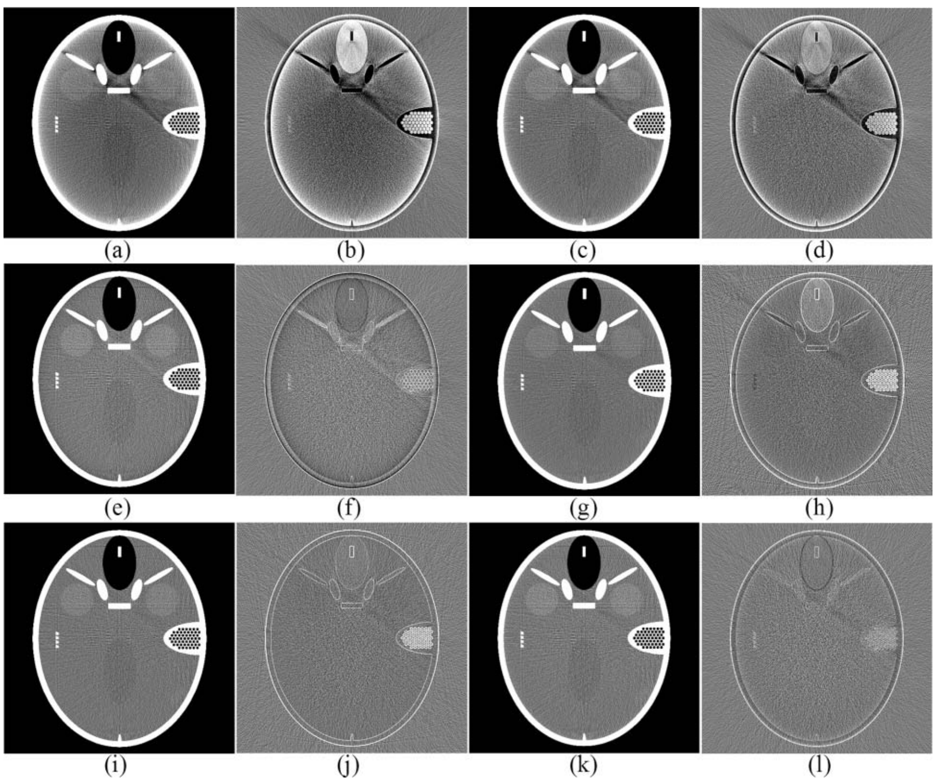

Fig. 12 Same as Fig. 11 but with noise in projection.

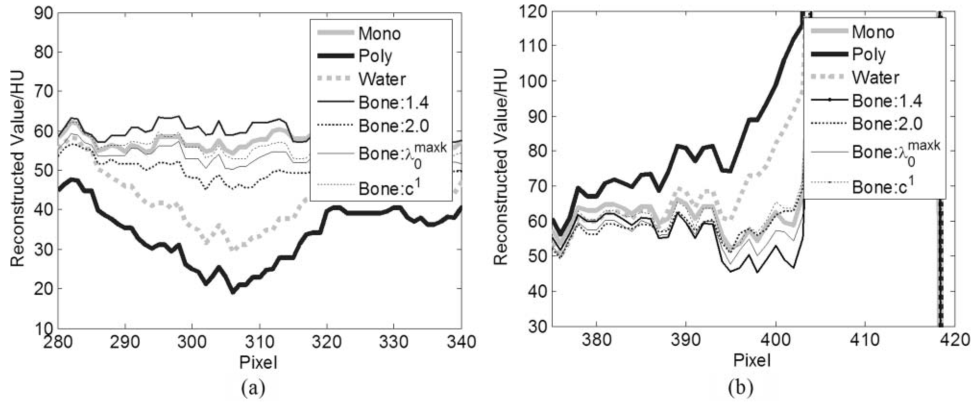

Fig. 13 Profiles of reconstructed images at $z = 0$ from noise-free projection. (a) and (b) are profiles along the horizontal 215th and 385th lines, respectively.

the inconsistency error in the soft-tissue region is always lower than in the bone-tissue region.

Figure 15 shows the effect of varying the number of photons on the inconsistency error, where the images (a) and (b) correspond to the bone- and soft-tissue regions, respectively. Figure 15 shows that the performance of the bone-correction with $\lambda_0^{\max k}$ follows closely to the bone-correction with λ_b. At the same time, it was not surprising that the bone-corrections with λ_b and λ_s are best in the bone- and soft-tissue regions, respectively. As for the bone-correction with $\boldsymbol{c}^1$, it was noticed that its inconsistency error in the soft-tissue region is acceptable, although its inconsistency error in the bone-tissue region is even larger than the bone-correction with λ_s. We believe that, given the comprehensive results in Figs. 11–15 and Table 2 and the lack of spectra data, the bone-correction with $\boldsymbol{c}^1$ is still uniquely valuable for a specific beam-hardening correction task.

5 Discussions

Previously, it has been asserted that, given all the schemes available for the choice of weight coefficient set $\{w_d \geq 0, d \in \mathbb{N}\}$, the scheme corresponding to the 0th order residual error term is the most essential for the minimization of objective function. Up to this point, the rationale underlying this assertion had still not been verified in a mathematical sense. However, we have observed from numerical simulations that there is no reasonable minimum value point in the objective function constructed based on the higher order residual error term (e.g., $w_d \neq 0$ iff $d = 1$). That is, there is no similar convergence phenomenon as is shown in Fig. 9.

In this article, we have proposed and implemented an algorithm to automatically determine the scaling factor $\lambda_0^{\max k}$ and coefficient vector $\boldsymbol{c}^1$ for bone-correction. During the beam-hardening correction for the polychromatic projection, we would never enforce the adoption of spectra $S(\varepsilon)$ and $Q(\varepsilon)$. If these spectra are not easily determined, the bone-correction with $\boldsymbol{c}^1$ can be efficiently adopted for a specific beam-hardening correction task.

In the bone-correction formula,

$$P_w \left\{ \ln \left[\int_{\varepsilon_{\min}}^{\varepsilon_{\max}} S(\varepsilon)\, Q(\varepsilon)\, d\varepsilon \Bigg/ \int_{\varepsilon_{\min}}^{\varepsilon_{\max}} S(\varepsilon)\, Q(\varepsilon)\, e^{-\mu_s(\varepsilon) g_s - \mu_b(\varepsilon) g_b / \lambda_0} d\varepsilon \right] \right\}$$

is essentially the water-corrected result of the estimated polychromatic projection (WEPP) with respect to g_s and g_b. After the logarithmic operation and water-correction, the WEPP is nearly a linear function of variables g_s and g_b. Therefore, an algebraic polynomial with respect to g_s and g_b (i.e., $[\, g_s \; g_b \; g_s^2 \; g_b^2 \; g_s g_b \; g_b^{0.5} \,] \cdot \boldsymbol{c}'$) is sufficient for the approximation to the WEPP. Also, other schemes can be used for this approximation task. For simplicity, in this article we have adopted the algebraic polynomial approximation, which is

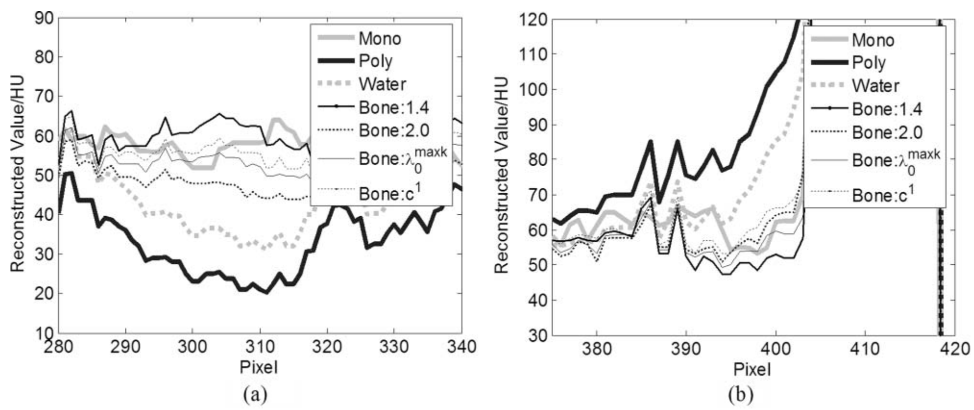

Fig. 14 Same as Fig. 13 but from noisy projection.

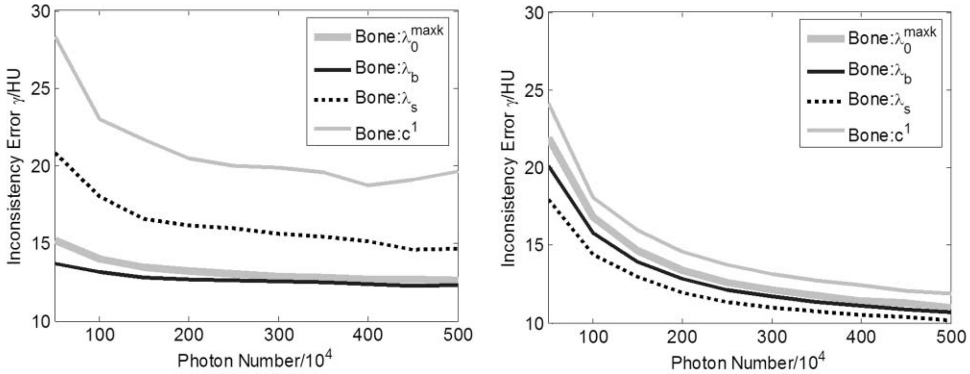

Fig. 15 Inconsistency errors versus the number of photons in the regions of (a) bone-tissue and (b) soft-tissue.

complete from the view-point of approximation theory. That is, a function can be approximated with an arbitrary accuracy, so long as the algebraic polynomial approximation is of an infinite order. However, the accuracy of an algebraic polynomial approximation is not sufficient when it is of only a finite order, which is equal to the dimension of coefficient vector c. The dimension limitation is required to improve the stability of the minimization of objective function. In order to improve the approximation accuracy, the term $g_b^{0.5}$ is added to the algebraic polynomial. It should be noted that the gain from this trick arises from the fact that the term $g_b^{0.5}$ is not a monomial basis of the algebraic polynomial approximation.

From Fig. 10(a), it can be seen that scaling factors λ_b and λ_s are dependent on the number of photons, while the dependency of λ_s is much larger than λ_b; in contrast, there is almost no dependency for $\lambda_0^{\max k}$. The lesser the number of photons the larger the difference between λ_b and λ_s is. From Fig. 8 and Table 1, we can also notice that scaling factors λ_b and λ_s are dependent on the cross-sectional position. From the previous two points, we can understand the difficulty of physical experiments to determine the scaling factor λ_0 (regardless of λ_b or λ_s) for bone-correction. As for $\lambda_0^{\max k}$, determined by our proposed method, it is very robust to the influences of both noise effects and cross-sectional position, and is nearly the optimal from the perspective of both the objective function $\mathbf{\Phi}_0$ in Fig. 10(b) and the inconsistency error γ in Fig. 15.

The ECC method has been proposed to correct for cupping artifacts,[17] which arise from a first-order beam-hardening effect. In ECC, a pre-correction function in polynomial form is utilized to approximate the beam-hardening effect of a homogeneous object such as soft-tissue. Recently, the EBHC method was proposed to correct simultaneously for cupping and streak artifacts,[26] which arise from a higher-order beam-hardening effect in a mixture of materials; EBHC has shown a capability for superior correction.

In EBHC, there is an approximation strategy similar to that used in this article. The relationship between our proposed method and EBHC is illustrated below. In our proposed method, after the determination of the coefficient vector c, the corrected projection is calculated according to the following formula,

$$g \approx P_w(\hat{g}) + g_w - \left[g_s \ g_b \ g_s^2 \ g_b^2 \ g_s g_b \ g_b^{0.5} \right] \cdot c', \tag{33}$$

where $g_w \triangleq g_s + g_b \approx P^w(\hat{g})$. So, we have

$$g \approx (2 - c_1) P_w(\hat{g}) + (c_1 - c_2) g_b + (2c_3 - c_5) P_w(\hat{g}) g_b + (c_5 - c_3 - c_4) g_b^2 - c_3 P_w(\hat{g})^2 - c_6 g_b^{0.5}. \tag{34}$$

Compared to the Eq. (4) in EBHC,[26] term by term, there exists the following relationship,

$$c_1 \approx 1, c_2 \approx 1 - c_{01}, c_3 \approx 0, c_4 \approx -c_{11} - c_{02}, c_5 \approx -c_{11}, c_6 \approx 0, P_w(\hat{g}) = p_0, g_b = p_2, \tag{35}$$

or

$$c_{01} \approx 1 - c_2, c_{11} \approx -c_5, c_{02} \approx c_5 - c_4, p_0 = P_w(\hat{g}), p_2 = g_b. \tag{36}$$

From Eqs. (35) and (36), it is easy to notice that the extra degrees of freedom can provide more accurate approximations in our proposed method. Additionally, in EBHC the combination weight set $\{c_{ij}\}$ is determined by minimizing the inflatness of the corrected volume. In other words, the determination of weight set in EBHC was performed in an

Table 2 The inconsistency errors γ in both the bone- and soft-tissue regions determined from the reconstructed images in Figs. 11 and 12.

Regions	Noise	Poly	Water	Bone:1.4	Bone:2.0	Bone:$\lambda_0^{\max k}$	Bone:c^1
Bone-tissue	Noise-free	33.2900	30.0313	20.3786	12.9694	12.1511	18.4233
	Noisy	33.4448	30.1666	21.2357	13.3265	12.8939	19.8651
Soft-tissue	Noise-free	17.8394	12.7992	10.4410	8.5776	9.0130	9.7519
	Noisy	20.0423	15.9094	14.0162	11.2117	12.1244	13.1492

image domain, whereas our proposed method accomplished this in projection domain.

It is noteworthy that our proposed method can also be carried out in spiral cone-beam CT and C-arm CT systems, once it is generalized into the corresponding geometries. Several possible alternatives for the H-L consistency condition have been available, such as fan-beam integral invariant,[45] fan-beam data consistency condition,[33,38] John's equation,[46–49] and the consistency condition derived from John's equation.[50] Another strategy is that the beam-hardening artifacts in spiral cone-beam CT or C-arm CT are corrected with the scaling factor λ_0 or coefficient vector c, which is determined by using a specific fan-beam projection data being sampled from the cone-beam projection data. Our proposed method can also be improved to adapt to the dynamic CT reconstruction in cardiac imaging[51–53] and the iterative reconstruction based on a statistical modeling for low-dosage XCT imaging.[54] As for the scattering component in the cone-beam geometries, a physical collimator or anti-scattering grid is considered to be beneficial to the implementation of our proposed method, although some modifications should be strengthened.

6 Conclusions

In this article, the influence of the scaling factor on the performance of bone-correction is analyzed. The results in the analysis illustrate that an optimal scaling factor does exist for bone-correction. Additionally, several critical factors in medical XCT systems, such as noise in projection data and cross-sectional position of imaged object, have been investigated to determine their impacts on the optimal scaling factor.

An algorithm is proposed to automatically determine the scaling factor. Differing from the original bone-correction method, which uses a large number of physical experiments to pre-determine the scaling factor, our proposed algorithm determines the scaling factor by combining the projection data consistency condition into an approximation process. Regardless of changes to imaging conditions, the approximation process can effectively solve the scaling factor. Our algorithm shows a high degree of robustness. Under conditions where no emitting and absorption spectra are available, an alternative algorithm with an algebraic polynomial approximation is also applicable. Further researches on practical medical XCT systems with physical compensators will be done in the near future.

Acknowledgments

This work was partially supported by the National Science Fund of China (No. 60551003), the program of NCET (No. NCET-05-0828), and the fund of the Ministry of Education of China (No. 20060698040).

Appendix: H-L Consistency Condition

In the equispatial fan-beam geometry, as shown in Fig. 1, defining a geometrical moment as

$$u_{j,k} \triangleq \int\int x^j y^k f(x, y)\, dx dy, j \geqslant 0, k \geqslant 0 \tag{A1}$$

and a projection moment as

$$V_d(\beta) \triangleq \int_{-\infty}^{+\infty} g\left(t, \beta - \tan^{-1}\frac{t}{D}\right)\left(\frac{tD}{\sqrt{D^2+t^2}}\right)^d \times \frac{D^3}{(D^2+t^2)^{1.5}} dt, d \geq 0. \tag{A2}$$

From the geometrical moment, we can construct the following quantity:

$$U_d(\beta) \triangleq \sum_{r=0}^{d} C_d^r u_{r,d-r} \cos^r \beta \sin^{d-r} \beta, q \geq 0. \tag{A3}$$

Then, there is an essential equality as follows:

$$V_d(\beta) = U_d(\beta), \tag{A4}$$

which is called the H-L consistency condition.[32,34,37,40,55] Particularly, when $d = 0$, there is

$$u_{0,0} = \int_{-\infty}^{+\infty} g\left(t, \beta - \tan^{-1}\frac{t}{D}\right) \frac{D^3}{(D^2+t^2)^{1.5}} dt, \tag{A5}$$

which is independent of the view-angle β.

References

1. J. Merbach, "Simulation of x ray projections for experimental 3D tomography," *Image Processing Lab, Department of Electrical Engineering*, (Linkoping University, Linkoping, Sweden, 1996).
2. B. De Man and S. Basu, "Distance-driven projection and backprojection," *IEEE Nuclear Science Symposium Conference Record* Vol. 3, 1477–1480 (2003).
3. H. Yu, S. Zhao, and G. Wang, "A differentiable Shepp-Logan phantom and its applications in exact cone-beam CT," *Phys. Med. Biol.* **50**, 5583–5595 (2005).
4. J. Zhu, S. Zhao, Y. Ye, and G. Wang, "Computed tomography simulation with superquadrics," *Med. Phys.* **32**, 3136–3143 (2005).
5. W. D. McDavid, R. G. Waggener, W. H. Payne, and M. J. Dennis, "Correction for spectral artifacts in cross-sectional reconstruction for x rays," *Med. Phys.* **4**, 54–57 (1977).
6. G. T. Herman, "Correction for beam hardening in computed tomography," *Phys. Med. Biol.* **24**, 81–106 (1979).
7. P. Joseph and R. Spital, "A method for correcting bone induced artifacts in computed tomography scanners," *J. Comput. Assist. Tomogr.* **2**, 100–108 (1978).
8. O. Nalcioglu and R. Y. Lou, "Post-reconstruction method for beam hardening in computerised tomography," *Phys. Med. Biol.* **24**, 330–340 (1979).
9. B. De Man, J. Nuyts, P. Dupont, G. Marchal, and P. Suetens, "Metal streak artifacts in x ray computed tomography: a simulation study," *IEEE Trans. Nucl. Sci.* **46**, 691–696 (1999).
10. S. Tang, H. Yu, H. Yan, D. Bharkhada, and X. Mou, "X ray projection simulation based on physical imaging model," *J. X Ray Sci. Tech.* **14**, 177–189 (2006).
11. S. Tang, X. Mou, Y. Yang, Q. Xu, and H. Yu, "Application of projection simulation based on physical imaging model to the evaluation of beam hardening corrections in x ray transmission tomography," *J. X-Ray Sci. Tech.* **16**, 95–117 (2008).
12. H. Z. Wang, "How to Read a Head CT," http://www.urmc.rochester.edu/smd/Rad/headct.htm (1999).
13. K. N. Paterakis, A. H. Karantanas, G. M. Hadjigeorgiou, V. Anagnostopoulos, and A. Karavelis, "Retroclival epidural hematoma secondary to a longitudinal clivus fracture," *Clinical Neurology and Neurosurgery* **108**, 67–72 (2005).
14. G. N. Hounsfield, British Patent No. 1283915 (British Patent Office, London, 1972).
15. R. A. Brooks and G. D. Chiro, "Beam hardening in x ray reconstructive tomography," *Phys. Med. Biol.* **21**, 390–398 (1976).
16. E. Casteele, D. V. Dyck, J. Sijbers, and E. Raman, "An energy-based beam hardening model in tomography," *Phys. Med. Biol.* **47**, 4181–4190 (2002)
17. M. Kachelrieß, K. Sourbelle, and W. A. Kalender, "Empirical cupping correction: A first-order raw data precorrection for cone-beam computed tomography," *Med. Phys.* **33**, 1269–1273 (2006).
18. P. M. Joseph and C. Ruth, "A method for simultaneous correction of spectrum hardening artifacts in CT images containing both bone and iodine," *Med. Phys.* **24**, 1629–1634 (1997).
19. C. H. Yan, R. T. Whalen, G. S. Beaupre, G. S. Yen, and S. Napel, "Reconstruction algorithm for polychromatic CT imaging: application to beam hardening correction," *IEEE Trans. Med. Imaging* **19**, 1–11 (2000).
20. B. De Man, J. Nuyts, P. Dupont, G. Marchal, and P. Suetens, "An iterative maximum-likelihood polychromatic algorithm for CT," *IEEE Trans. Med. Imaging* **20**, 999–1007 (2001).

21. I. A. Elbakri and J. A. Fessler, "Segmentation-free statistical image reconstruction for polyenergetic x ray computed tomography with experimental validation," *Phys. Med. Biol.* **48**, 2453–2477 (2002).
22. J. Hsieh, R. C. Molthen, C. A. Dawson, and R. H. Johnson, "An iterative approach to the beam hardening correction in cone beam CT," *Med. Phys.* **27**, 23–29 (2000).
23. X. Mou, S. Tang, and H. Yu, "Comparison on beam hardening correction of CT-based HL consistency and normal water phantom experiment," *Proc. SPIE* **6318**, 63181V (2006).
24. X. Mou, S. Tang, and H. Yu, "A beam hardening correction method with HL consistency," *Proc. SPIE* **6318**, 63181U (2006).
25. X. Mou, S. Tang, T. Luo, Y. Zhai, and H. Yu, "Beam hardening correction based on HL consistency in polychromatic transmission tomography," *Proc. SPIE* **6913**, 691333 (2008).
26. Y. Kyriakou, E. Meyer, D. Prell, and M. Kachelrieß, "Empirical beam hardening correction (EBHC) for CT," *Med. Phys.* **37**, 5179–5187 (2010).
27. G. Christ, "Exact treatment of the dual-energy method in CT using polyenergetic x ray spectra," *Phys. Med. Biol.* **29**, 1501–1510 (1984).
28. A. J. Coleman and M. Sinclair, "A beam-hardening correction using dual-energy computed tomography," *Phys. Med. Biol.* **30**, 1251–1256 (1985).
29. E. Y. Sidky, Y. Zou, and X. Pan, "Impact of polychromatic x ray sources on helical cone-beam computed tomography and dual-energy methods," *Phys. Med. Biol.* **49**, 2293–2303 (2004).
30. M. Li and D. Wang, "CT image reconstruction from limited information," *Proc. SPIE* **2390**, 116–126 (1995).
31. S. Basu and Y. Bresler, "Uniqueness of tomography with unknown view angles," *IEEE Trans. Image Process.* **9**, 1094–1106 (2000).
32. H. Yu, X. Mou, and Y. Cai, "Calibration of cone beam rotational x ray image sequence," *Chin. J. Electron.* **13**, 424–428 (2004).
33. G. Chen and S. Leng, "A new data consistency condition for fan-beam projection data," *Med. Phys.* **32**, 961–967 (2005).
34. H. Yu, Y. Wei, J. Hsieh, and G. Wang, "Data consistency based translational motion artifact reduction in fan-beam CT," *IEEE Trans. Med. Imaging* **25**, 792–803 (2006).
35. S. Schröder, I. Stuke, and T. Aach, "On interpolation of sparsely sampled sinograms," *Proc. SPIE* **6144**, 61446S (2006).
36. G. V. Gompel, M. Defrise, and D. V. Dyck, "Elliptical extrapolation of truncated 2D CT projections using Helgason-Ludwig consistency conditions," *Proc. SPIE* **6142**, 1424B (2006).
37. H. Yu and G. Wang, "Data consistency based rigid motion artifact reduction in fan-beam CT," *IEEE Trans. Med. Imaging* **26**, 249–260 (2007).
38. S. Leng, B. Nett, M. Speidel, and G. Chen, "Motion artifact reduction in fan-beam and cone-beam computed tomography via the Fan-beam data consistency condition (FDCC)," *Proc. SPIE* **6510**, 65101W (2007).
39. J. Xu, K. Taguchi, and B. M. W. Tsui, "Statistical projection completion in x ray CT using consistency conditions," *IEEE Trans. Med. Imaging* **29**, 1528–1540 (2010).
40. F. Natterer, *The Mathematics of Computerized Tomography*, (John Wiley & Sons, New York, 1986).
41. G. Wang, T. H. Lin, P. Cheng, and D. M. Shinozaki, "A general cone-beam reconstruction algorithm," *IEEE Trans. Med. Imaging* **12**, 486–496 (1993).
42. T. R. Fewell, R. E. Shuping, and K. R. Hawkins, "Handbook of computed tomography x ray spectra," Washington, D.C.: HHS Publication (FDA), **81-8162**, 27–29 (1981).
43. J. A. Rowlands and K. W. Taylor, "Absorption and noise in cesium iodide x ray image intensifiers," *Med. Phys.* **10**, 786–795 (1983).
44. G. Lauritsch and H. Bruder, "head phantom," http://www.imp. uni-erlangen.de/phantoms/head/head.html, (1998).
45. Y. Wei, H. Yu, and G. Wang, "Integral indifferents for computed tomography," *IEEE Signal Process. Lett.* **13**, 549–552 (2006).
46. F. John, "The ultrahyperbolic equation with four independent variables," *J. Duke Math* **4**, 300–322 (1938).
47. S. K. Patch, "Computation of unmeasured third-generation VCT views from measured views," *IEEE Trans. Med. Imaging* **21**, 801–813 (2002).
48. S. K. Patch, "Consistency conditions upon 3D CT data and the wave equation," *Phys. Med. Biol.* **47**, 1–14 (2002).
49. M. Defrise, F. Noo, and H. Kudo, "Improved two-dimensional rebinning of helical cone-beam computerized tomography data using John's equation," *Inverse Probl.* **19**, S41–S54 (2003).
50. M. S. Levine, E. Y. Sidky, and X. Pan, "Consistency conditions for cone-beam CT data acquired with a straight-line source trajectory," *Proc. 10th Int. Meeting on Fully Three-Dimensional Image Reconstruction in Radiology and Nuclear Medicine*, Beijing, China, September 5–10, 2009, pp. 102–105 (2009).
51. G. Chen, J. Tang, and S. Leng, "Prior image constrained compressed sensing (PICCS): A method to accurately reconstruct dynamic CT images from highly undersampled projection data sets," *Med. Phys.* **35**, 660–663 (2008).
52. G. Chen, J. Tang, and J. Hsieh, "Temporal resolution improvement using PICCS in MDCT cardiac imaging," *Med. Phys.* **36**, 2130–2135 (2009).
53. J. Tang, J. Hsieh, and G. Chen, "Temporal resolution improvement in cardiac CT using PICCS (TRI-PICCS): Performance studies," *Med. Phys.* **37**, 4377–4388 (2010).
54. J. Tang, B. Nett, and G. Chen, "Performance comparison between total variation (TV)-based compressed sensing and statistical iterative reconstruction algorithms," *Phys. Med. Biol.* **54**, 5781–5804 (2009).
55. A. K. Louis and A. Rieder, "Incomplete data problems in x ray computerized tomography," *Numer. Math.* **56**, 371–383 (1989).

Biographies and photographs of the authors not available.